Visualisation of moderate Reynolds number flow through a tooth-shaped nozzle

X. Grandchamp (1) A. Van Hirtum (1,2) K. Nozaki (3) J. Cisonni (3) X. Pelorson (1) and S. Shimojo (4)

(1) Gipsa-lab, UMR CNRS 5216, Grenoble Universities, France
(2) Cybermedia Center, Osaka University, Japan
(3) The Center for Advanced Medical Engineering and Informatics, Osaka University, Japan
(4) National Institute of Information and Communications Technology, Japan

ABSTRACT

The spatial development of steady flow through a constricted rectangular nozzle is characterised. The constriction consists of an obstacle in the shape of a trapezoid wedge, which is inserted perpendicular to the main flow direction. The channel exit is situated downstream the obstacle at 1.5 times the minimum aperture. The constriction degree is fixed to 70% and the aspect ratio is 4 in the unconstricted and 15 in the constricted portion of the channel so that the flow is considered two-dimensional. The imposed bulk Reynolds number Re_b yields 4000. The flow through the channel is computed by Large Eddy Simulation. In addition, the flow through the nozzle downstream the obstacle up to 7 times the minimum aperture is experimentally assessed by smoke visualisation. As a consequence of the geometrical asymmetry in the nozzle design, important asymmetries in mean as well as shear flow development are pointed out. Despite severe simplifications, the studied nozzle geometry and flow conditions are relevant to human fricative production.

INTRODUCTION

Engineering applications of jet flow are many: combustion, mixing, cooling, drying, *etc*. A far less evident application is the study of jet flow in relation to upper airway flow. Although, since the sixties Fant (1960), jet flow is known to be a basic ingredient of fricative production for which the underlying mechanism is described as: noise produced due to the interaction of a *turbulent jet*, generated at a constriction somewhere in the vocal tract, with a *downstream wall or obstacle* Howe and McGowan (2005), Ramsay (2008), Shadle (1985). Nevertheless, studies dealing with the characterisation of the flow covering configurations relevant to human fricative production, *i.e.* moderate bulk Reynolds number $2000 < Re_b < 10^4$ and low Mach number $Ma < 1$, are lacking, as pointed out in Howe and McGowan (2005). Recently, single sensor anemometry was applied to characterise the spatial velocity distribution issuing from an extended conical diffuser representing a constriction 'somewhere' between the tongue and the palatal palate ($Re_b = 7350$) Van Hirtum et al. (2009). The influence of the initial velocity profile at the tube exit on downstream jet development was assessed and the application of self-similar jet flow models was discussed. Although, no obstacle was considered. Therefore, jet flow development through a rectangular channel with a teeth-shaped obstacle inserted was recently studied ($Re_b = 4000$) Van Hirtum et al. (2010). Simulated and measured transverse velocity profiles in the near field downstream the teeth edge, from $0 \leq x/h \leq 1.5$ with aperture height $h = 7.5$mm and constriction degree 70%, were compared. The flow in the near field region was basically thought of as a two-layer shear flow consisting of an inner layer (similar to a boundary layer) and an outer layer (similar to a free shear layer). Consequently, mean and turbulent near field velocity profiles were characterised by considering flow parameters inspired on plane wall jet studies Eriksson et al. (1998). From the quantified features it was observed that the interaction between the two generic layers, *i.e.* inner layer and outer layer, leads to a

more complex near flow field. In order to increase understanding and characterisation of the flow structure, an overview of the spatial flow development is searched in the current study by visualisation of the simulated and experimental flow field. Besides application in the field of fricative speech production, the studied flow is a basic building block flow and therefore of considerable fundamental interest.

TOOTH-SHAPED NOZZLE

The geometry of the tooth-shaped nozzle is based on two main morphological characteristics: (1) upper incisor dimensions in the flow direction and (2) upper teeth position with respect to the palatal plane. The nozzle is schematically depicted in Fig. 1 Van Hirtum et al. (2010).

Briefly, the nozzle consists of a tooth-shaped obstacle inserted in a rectangular channel. The uniform channel has width $w = 105$mm, unconstricted channel height $h = 25$mm and total length l_{noz}. The tooth-shaped obstacle consists of a trapezoid defined by its base $l_{pal} = 6.6$mm Ellis and McNamara (1986), tip length $l_t = 1.25$mm Rudolph et al. (1998) and height $h_t = 17.5$mm Magne et al. (2003). The base of the trapezoid is a portion of the palatal plane represented by the upper plane of the rectangular channel. Consequently, when inserting the obstacle in the unconstricted channel, the leading and trailing angles of the tooth-shaped obstacle with the upper plane of the rectangular channel are $\theta_1 = 107°$ and $\theta_2 = 90°$ which corresponds to the order of magnitudes reported for *in-vivo* subjects Ellis and McNamara (1986), Fredericks (1974). Next, the tooth-shaped obstacle is inserted $l_0 = 11$mm upstream of the nozzle outlet in order to respect the morphological distance between the trailing teeth edge and the trailing lip position approximated as $l_0 \approx 1.7 \times l_{pal}$ McIntyre and Millett (2006). The resulting minimum aperture at the obstacle yields $h = h_0 - h_t = 7.5$mm.

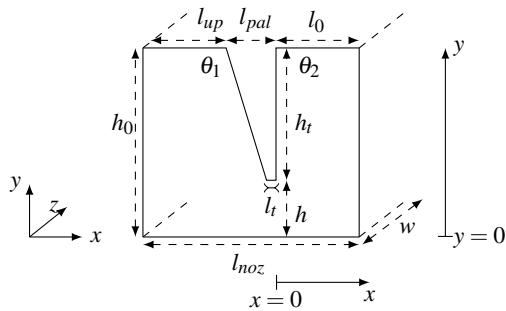Figure 1: Schematic representation of the *in-vitro* tooth-shaped nozzle: unconstricted channel height $h_0 = 25$mm, uniform channel width $w = 105$mm, minimum aperture height $h = 7.5$mm, obstacle height $h_t = 17.5$mm, obstacle tip length $l_t = 1.25$mm, obstacle base length $l_{pal} = 6.6$mm, length from the obstacle trailing edge up to the nozzle outlet $l_0 = 11$mm, length from the nozzle inlet to the obstacle leading edge l_{up}, total nozzle length $l_{noz} = l_{up} + l_{pal} + l_0$, $\theta_1 = 107°$ and $\theta_2 = 90°$ the obstacles leading and trailing edge angles. The x-axis corresponds to the main flow direction.

The aspect ratios of the resulting tooth-shaped nozzle, both in the unconstricted and constricted region, are superior to 1, $w/h_0 \approx 4$ and $w/h \approx 15$. Consequently, the flow is expected to be statistically similar to two-dimensional flow Mi et al. (2005). The contraction ratio h_0/h yields ≈ 3.3 resulting in a $\pm 70\%$ obstruction degree at the tooth obstacle. The ratios of 1) the obstacle length l_{pal} and 2) the channel downstream the constriction l_0 to the minimum aperture yield $l_{pal}/h = 0.88$ and $l_0/h = 1.5$.

METHODOLOGY

Smoke visualisation setup

In order to enable smoke visualisation experiments, a suitable rigid *in-vitro* replica of the nozzle depicted in Fig. 1 is obtained by inserting a plain obstacle in a transparent rectangular channel, instead of the plaster model used in Van Hirtum et al. (2010). Different nozzles are obtained by accounting for different lengths l_{up} (5, 36 and 67cm), and consequently l_{noz}, upstream of the obstacle. Experimental variation of l_{up} is motivated since entrance flow in a sharp-edged channel is likely to develop and might influence the flow at the channel exit Sadri and Floryan (2002), Wilson (1971). In addition, sensitivity of the flow development to entrance conditions is in particular important when aiming aero-acoustic applications involving noise production such as fricative speech production Bogey and Bailly (2005). Besides the total nozzle length l_{noz}, the dimensions of the *in-vitro* replica match the tooth-shaped nozzle described earlier. The transparent walls of the *in-vitro* replica have thickness $th = 5.5$mm.
The air through and downstream of the *in-vitro* replica is visualised by smoke injection. The experimental setup is schematically represented in Fig. 2.

Neutrally buoyant white smoke (Steinigke Showtechnic GmbH, fluid smoke, polyglycol, glycerol, 3-ethyleenglycol, 1.2 propyleneglycol in water double destilled water, 1.06 g/cm^3) is injected in a settling chamber with volume 0.112m^3 by means of a fog machine (Kool Light, FOG-1200E, 1200W, maximum volume flowrate 300 m^3/min). Grids are used in the settling chamber in order to reduce the turbulence intensity so that the streamwise turbulence intensity at the nozzle inlet is below 1% Van Hirtum et al. (2010).
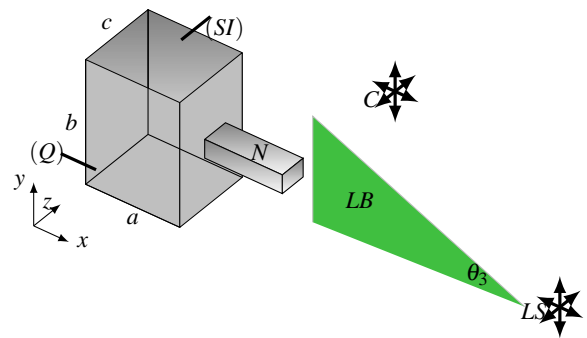

Figure 2: Schematic representation of the experimental setup: 1) settling chamber of volume 0.112m^3 with dimensions $56 \times 50 \times 40$cm ($a \times b \times c$) to which the nozzle (N) represented in Fig. 1 is attached, 2) smoke injection inlet (SI), 3) volume airflow rate supply (Q), 4) laser source (LS) with cylindrical lens resulting in a diverging ($\theta_3 = 10°$) laser beam (LB). 5) high speed camera (C) perpendicular to the laser beam. The laser source (LS) and camera (C) are mounted on a three-dimensional rail system. The axes are as defined in Fig. 1, so that the x-axis indicates the main flow direction and the y-axis the transverse direction. Gravity is in the z-direction. An example of a two dimensional (x,y) instantaneous flow visualisation image for $Re_b = 4000$ is shown in Fig. 3.
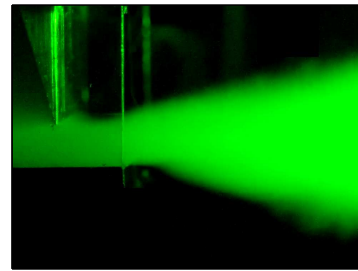

Figure 3: Example of two dimensional (x,y) instantaneous flow visualisation image for $Re_b = 4000$.

Two-dimensional illumination is applied with a two-dimensional laser light beam. The laser light beam is generated by a class IIIb laser light source (Laserglow Technologies, LRS--0532-TFM-00200-10, 234.2mW, wavelength of 532nm and with spectral linewidth < 0.1nm) to which a 10 degree cylindrical lens is added. The resulting beam has a thickness of 1mm. To record the illuminated smoke pattern, a color camera (Casio, EXILIM Pro EX-F1, 6.0 million effective pixels and a 12X optical zoom) was positioned perpendicular to the laser sheet on a three dimensional rail system in order to facilitate the recording. The back wall of the test chamber was painted in black to ensure a good contrast with the smoke pattern. Movies are recorded at 30fps. So, the time interval between consecutive images is 0.033s. The digitised images are 720×1280 data matrices. Spatial calibration of the images is performed.
Airflow is generated in a flow facility consisting of an air compressor (Atlas Copco GA7) followed by a manual valve and pressure regulator (Norgren type 11-818-987) enabling one to provide constant air pressure. A uniform duct of diameter 1cm connects the pressure regulator to the smoke reservoir enabling to visualise smoke patterns for a chosen volume airflow rate. In the current experiment, the volume airflow rate is fixed to $Q = 363$l/min corresponding to bulk Reynolds number $Re_b = 4000$.

Numerical simulation: mesh and boundary conditions

The airflow is simulated with Large Eddy Simulation (LES) for incompressible unsteady flows. The dynamic Smagorinsky model (DSM) Germano et al. (1991) with modification due to Lilly Lilly (1992) is used so that the Smagorinsky coefficient C_s in the viscosity function is determined locally in space and time from the smallest resolved scales from which the eddy viscosity is determined. Simulations are obtained with a general-purpose finite element code *Front Flow Blue/FFB5* Guo et al. (2006), Kato and Ikegawa (1991) on a supercomputer (SX8 NEC Inc.). Simulation results are visualised with commercial software (FieldView v12, VINAS Inc.).

The computational nozzle matches the tooth-shaped nozzle exactly. The inlet length of the channel is set to $l_{up} = 92.4$mm, so that the total length of the computational channel yields $l_{noz} = 110$mm.

The computational mesh is a structured multiblock grid (Gridgen v1.5, Pointwise Inc.) of 1 882 200 hexahedral elements composed out of 5 regions as illustrated in Fig. 4. The blocks are defined in Table 1. The quality of the mesh was verified
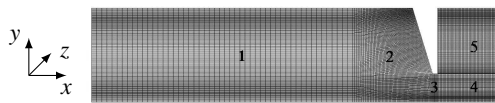

Figure 4: Computational multiblock grid of 1 882 200 hexahedral elements composed out of 5 regions defined in Table 1. Axes are defined as indicated in Fig. 1.

	block 1	block 2	block 3	block 4	block 5
z	40	40	40	40	40
y	191	191	62	62	100
x	52	105	14	100	100
total	397280	802200	34720	248000	400000

Table 1: Number of elements for each block: $z \times y \times x$ (or width $\times$ height $\times$ length) as defined in Fig. 4. The total number of elements yields 1882200.

with respect to minimum vertex angle, maximum face skewness, minimum element size and node distribution. Although the mesh sensitivity of the simulation was not explicitly tested, the element density is assumed to be sufficient since 1) the total number of elements is of order 10^6 which is large seen the dimensions of the problem and 2) as seen from Fig. 4 the element density is increased 'at' as well as 'downstream' of the constriction resulting in a fine grid with averaged precision < 0.13mm in the main flow direction. The grid precision is further increased to 0.05mm along the boundaries. The grid precision along the z direction is much less as along the x and y dimension since due to the large aspect ratio a two-dimensional flow is assumed. The assumption is validated by anemometry on a plaster model of the computational grid (3D Digital Service OURA Inc.) Van Hirtum et al. (2010).

A uniform velocity profile is imposed at the inlet of the computational domain. No-slip boundary conditions are used at the wall whereas zero pressure is imposed at the outlet. The Reynolds number is set to match experimental conditions, i.e. $Re_b = 4000$, so that the bulk velocity yields $U_b = 2.4$m/s and the volume airflow rate $\phi = 363$l/min. The non-dimensional time increment Δt is set so that $10^{-3} = \Delta t \cdot U_b / h_0$ with U_b the bulk velocity at the inlet and h_0 the unconstricted nozzle height in accordance with Fig. 1. Mean and fluctuating characteristics of the velocity field are quantified on 5000 instantaneous flow fields or 0.052s obtained from time step 5000 up to 10000.

An accurate grid in combination with a dynamic Smagorinsky

model is used in order to ensure the quality of the computational simulation. This is further confirmed by the evolution of the Courant-Friedrichs-Lewy condition (CFL) which is evaluated during simulation. The CFL-number remains constant after 3000 time steps and its value yields 0.6, which is well below 1. The value of the C_s coefficient is low ($C_s < 0.002$) everywhere, except near the jet edges where $C_s < 0.022$. In addition, from the filtered velocity field in the main flow direction, *i.e.* the *x*-component, it is seen that the sub-grid scale contribution is about 9%. Consequently, the contribution of the sub-grid scale model to the energy spectrum is assumed satisfying.

SPATIAL FLOW VISUALISATION

Simulated flow field

The x and y component of the simulated mean velocity flow field are illustrated in Fig. 5. The x component is seen to accelerate in the main streamwise direction from 2.4m/s at the inlet up to a maximum of 13m/s downstream the constriction. The negative velocities downstream of the trailing obstacle edge indicate the presence of a recirculation zone characterised by a negative pressure gradient. The computed y component of the mean velocity yields almost everywhere in the computational space the imposed value of 0m/s at the inlet, except just upstream at the leading edge of the obstacle where the negative values up to -8m/s are reached due to the acceleration towards the constriction. The z component is omitted in Fig. 5 since its mean value over the whole spatial domain is in the range $[-0.5\ 0.5]$m/s. The strong variation of both x and y component of the mean velocity in the vicinity of the obstacle results in an increased vorticity value at the obstacle tip.
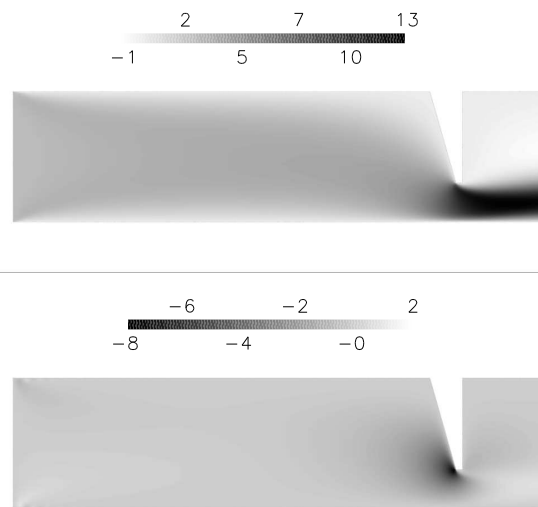

Figure 5: Simulated mean velocity for the plane $(x, y, z = w/2)$ and $Re_b = 4000$.

The spatial distribution of the x and y components of the turbulence intensities is illustrated in Fig. 6. As for the mean velocity, the z component is omitted since its values are neglectable (inferior to 1% for the whole spatial domain). The flow is seen to remain laminar upstream from the constricted channel portion. The y component of turbulence intensity increases locally at the upstream leading edge of the constriction up to 8%. The x component of the turbulence intensity increases up to 14% in the jet downstream the constriction.
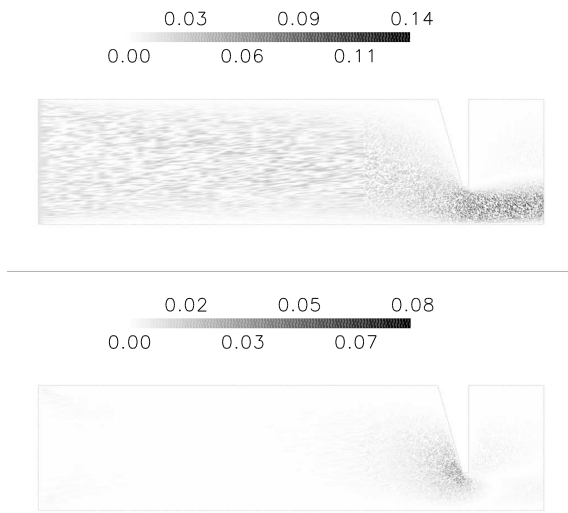
Figure 6: Simulated turbulence intensities for the plane $(x, y, z = w/2)$ and $Re_b = 4000$.

Experimental flow field

Individual images, such as shown in Fig. 3, are processed in order to estimate the instantaneous spatial distribution of smoke concentration from the scattered light intensity following standard methods Haralick and Shapiro (1992), Merzkirch (1987). Next, the mean and fluctuation (rms) portion of smoke concentration is calculated on consecutive images in order to 1) characterise spatial flow development up to $0 < x/h < 7$ and 2) in order to allow comparison between experimental and simulated flow field in the near field downstream the obstacle, *i.e.* $0 < x/h < 1.5$. Contour plots of the mean and rms spatial development of smoke concentration obtained from images acquired during 10s consecutively, are illustrated in Fig. 7.

From Fig. 7 is observed that the outer free shear layer on the obstacle side starts to develop upstream from the nozzle exit at $x/h < 1.5$ whereas the presence of the bottom plate up to $x = 1.5$ prevents the development of a free shear layer in this region. Consequently, the free shear layer at the wall side, develops downstream the nozzle exit resulting in a spatial asymmetry in shear layer development. From Fig. 7 the spatial asymmetry of the shear layer is seen to be accompanied by a spatial asymmetry of the mean flow development with a transverse shift at $x/h \approx 4.5$.

The smoke concentration in the near field downstream the obstacle for $0 < x/h < 1.5$ and $0 < y/h < 1$ is detailed in Fig. 8. The mean and rms spatial development downstream the obstacle in the region $0 < x/h < 1$ are both seen to be characterised by a transversal asymmetry which exhibits a maximum around $y/h \approx 0.8$. At the exit of the nozzle, *i.e.* $x/h = 1.5$, the transverse profile is seen to be approximatively uniform for $0 < y/h < 0.8$.

DISCUSSION

It needs to be specified that shown smoke visualisation experiments are obtained with channel length $l_{up} = 36$cm. Experimental variation of l_{up} to 5 or 67cm did not influence the experimental findings obtained from smoke visualisation. Therefore, the upstream sharp edge nozzle inlet is assumed to be of no influence due to the low turbulence intensity at the channel inlet
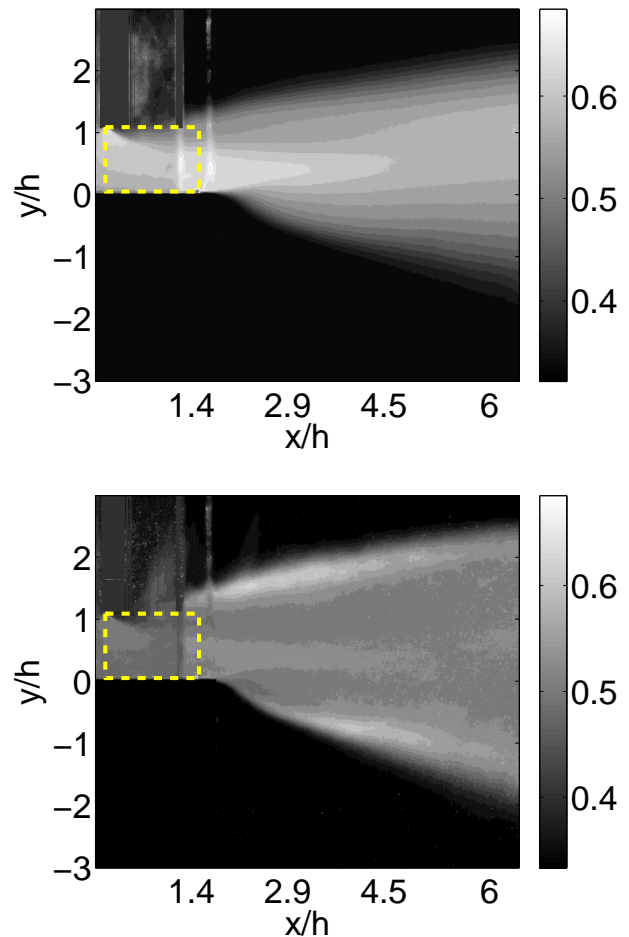

Figure 7: Contour plots of smoke concentration illustrating the spatial development of mean and fluctuating flow portion for $Re_b = 4000$ from instantaneous images captured during 10s consecutively. The near field - indicated by a dashed line in the overall image - from the obstacle up to the nozzle exit, *i.e.* $0 < x/h < 1.5$ and $0 < y/h < 1$, is detailed in Fig. 8.

and due to the presence of the obstacle further downstream. Visualisation of both simulated velocity data and experimental smoke patterns indicates a strong asymmetry of both the mean and rms flow development immediately downstream the obstacle, *i.e.* $0 < x/h < 1.5$. Therefore the current smoke experiments confirm and complement previous experimental point observations made on transverse measurement stations by hotfilm anemometry in this region Van Hirtum et al. (2010). The strong flow asymmetry is the result of the geometrical channel asymmetry between the obstacle and flat wall, resulting in a non-uniform flow acceleration towards the constriction due to the presence of the obstacle on one side and a flat channel wall at the other side. The transverse asymmetry of the mean jet in this near obstacle region is seen to be flattened towards the nozzle exit. On the contrary, the asymmetry in shear layer development is observed to increase towards the nozzle exit. The jet leaving the constriction remains unbounded on the obstacle side whereas it is bounded on the other side due to the presence of the flat channel wall, which prevents free shear layer development in favour of boundary shear layer development. Therefore, the development of the free shear layer on the flat wall side is shifted to downstream the nozzle exit instead of downstream the obstacle as is the case on the obstacle side. Performed smoke visualisation experiments allow to complement the simulated flow field in the region downstream the nozzle exit, *i.e.* $1.5 < x/h < 7$ and therefore to gain insight in the
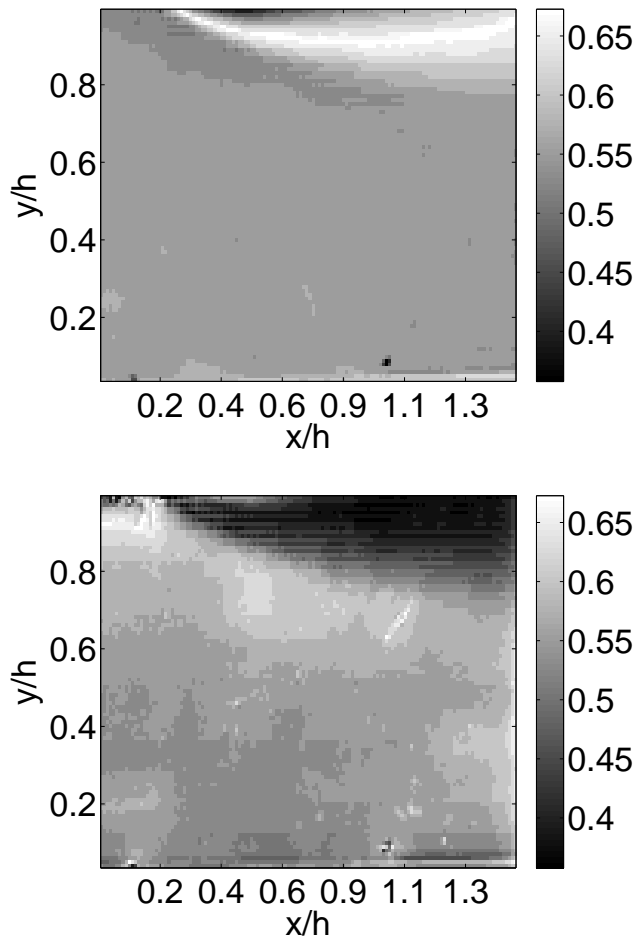
Figure 8: The mean and fluctuating portion of the near field - indicated by a dashed line in the overall image of Fig. 7 - from the obstacle up to the nozzle exit, i.e. $0 < x/h < 1.5$ and $0 < y/h < 1$, is detailed.

spatial development of the shear layer interaction. Due to the mentionned spatial shift in free shear layer development initiated in the region upstream the nozzle exit, i.e. $0 < x/h < 1.5$, the observed spatial asymmetry in rms is expected. In addition, smoke visualisation shows that the asymmetry in shear development entrains an asymmetry in mean flow development downstream the nozzle exit and this despite the loss of asymmetry in the transverse mean profile at the nozzle exit at $x/h = 1.5$ compared to the profile at the constriction $x/h = 0$ as is observed from simulation, smoke visualisation as well as previously by hot-film anemometry Van Hirtum et al. (2010).

The recirculation zone retrieved in the numerical flow data is experimentally observed on instataneous images. Nevertheless, it's appearance is not further discussed since it can not be characterised on the averaged flow visualisations.

In general, the performed smoke visualisation provides a spatial overview of the mean and shear spatial flow development downstream the obstacle. Therefore, the current study confirms - at least qualitatively - results of previous point measurements by hot-film anemometry as well as the general tendencies observed from visualisation of simulated data in the region downstream the obstacle up to the nozzle exit. In addition, since the development of the shear layers and mean flow downstream the nozzle exit is characterised as well, the current results are valuable for the design and validation of future experimental as well as numerical studies dealing with moderate Reynolds flow through asymmetrical nozzles. Therefore, presented results aim to contribute both to understanding of flow develope-

ment as its applications.

The found asymmetry in the flow development in the region $0 < x/h < 7$, so both upstream and downstream the nozzle exit, is likely to introduce vorticity upstream, as retrieved by numerical simulation, as well as downstream the nozzle exit, which is an important finding when sound production is of interest such as is the case for human fricative production for which related experimental flow data are few and necessary Howe and McGowan (2005), Krane (2005). In addition, knowledge of the spatial development of free shear layers is important with respect to the location of turbulence sound sources Lighthill (1954).

CONCLUSION

The current study presents numerical and experimental characterisation of the spatial development flow through an asymmetrical nozzle, i.e. constricted rectangular channel, at moderate bulk Reynolds number, $Re_b = 4000$. The simulation study of flow through the channel is complemented by smoke visualisation of flow downstream the obstacle including free space downstream the nozzle exit. The geometrical asymmetry is shown to cause important asymmetries in the spatial development of mean and shear flow development in the channel downstream the obstacle as well downstream the nozzle exit. The importance of the found asymmetries with respect to aero-acoustic sound sources is pointed out. Despite severe simplifications, current flow visualisation results contribute to the characterisation of the flow field during human fricative production since both flow and geometrical conditions are relevant. In addition, current results encourage future numerical and experimental studies.

ACKNOWLEDGEMENTS

REFERENCES

C. Bogey and C. Bailly. Effects of inflow conditions and forcing on subsonic jet flows and noise. *AIAA J.*, 43:1000–1007, 2005.

E. Ellis and J.A. McNamara. Cephalometric evaluation of incisor position. *Angle Orthod.*, 56:324–344, 1986.

J. Eriksson, R. Karlsson, and J. Person. An experimental study of a two-dimensional plane turbulent wall jet. *Exp. Fluids.*, 20:50–60, 1998.

G. Fant. *The acoustic theory of speech production*. Mouton, The Hague, 1960.

Collaborative Research Center for Computational Science and Technology. *FrontFlowBlue version 5.0 User Manual*. Institue of Industrial Science, The University of Tokyo, Japan, 2009.

C.D. Fredericks. A method for determining the maxillary incisor inclination. *Angle Orthod.*, 44:341–345, 1974.

M. Germano, U. Piomelli, P. Moin, and W. Cabot. A dynamic subgrid-scale eddy viscosity model. *Phys Fluids A*, 3:1760–1765, 1991.

Y. Guo, C. Kato, and Y. Yamade. Basic features of the fluid dynamics simulation software FrontFlow/Blue. *JSFM*, 58: 11–15, 2006.

R. Haralick and L. Shapiro. *Computer and robot vision*. Addison-Wesley Publishing Company, 1992.

M. Howe and R. McGowan. Aeroacoustics of [s]. *Proc. R. Soc. A*, 461:1005–1028, 2005.

C. Kato and M. Ikegawa. Large eddy simulation of unsteady turbulent wake of a circular cylinder using the finite element method. *ASME-FED*, 117:49–56, 1991.

M. Krane. Aeroacoustic production of low-frequency unvoiced speech sounds. *J. Acoust. Soc. Am.*, 118(1):410–427, 2005.

M. Lighthill. On sound generated aerodynamically: II. Turbulence as a source of sound. *Proc. R. Soc. A*, 222:1, 1954.

D. Lilly. A proposed modification of the Germano subgrid-scale closure method. *Phys. Fluids A*, 4:633–635, 1992.

P. Magne, G.O. Gaulluci, and U.C. Belser. Anatomic crown width/length ratios of unworn and worn maxillary teeth in white subjects. *The journal of prosthetic dentistry*, 89:453–461, 2003.

G.R. McIntyre and D. T. Millett. Lip shape and position in class ii division 2 malocclusion. *Angle Orthod.*, 76:739–744, 2006.

W. Merzkirch. *Flow visualisation*. Academic Press, London, UK, 1987.

J. Mi, R. Deo, and G. Nathan. Characterization of turbulent jets from high-aspect-ratio rectangular nozzles. *Phys. Fluids*, 17:4, 2005.

G. Ramsay. The influence of constriction geometry on sound generation in fricative consonants. In *Proc. Acoustics08*, pages 1–4, Paris, France, 2008.

D.J. Rudolph, P.D. Dominguez, K. Ahn, and T. Thinh. The use of tooth thickness in predicting intermaxillary tooth-size discrepancies. *Angle Orthod.*, 68:133–140, 1998.

R.M. Sadri and J.M. Floryan. Entry flow in a channel. *Computers & Fluids*, 31:133–157, 2002.

C. Shadle. *The acoustics of fricative consonants*. PhD thesis, 1985.

A. Van Hirtum, X. Grandchamp, and X. Pelorson. Moderate Reynolds number axisymmetric jet development downstream an extended conical diffuser: influence of extension length. *Eur. J. Mech - B/FLUIDS*, 28:753–760, 2009.

A. Van Hirtum, X. Grandchamp, X. Pelorson, K. Nozaki, and S. Shimojo. Large Eddy Simulation and 'in-vitro' experimental validation of flow around a teeth-shaped obstacle. *Int. J. of Applied Mechanics*, In press:1–12, 2010.

S.D.R. Wilson. Entry flow in a channel. part 2. *J. Fluid Mechanics*, 46(1):787–799, 1971.